Available online at www.sciencedirect.com
SCIENCE DIRECT
Journal of Power Sources 156 (2006) 388–399
JOURNAL OF POWER SOURCES
www.elsevier.com/locate/jpowsour

Toward the optimization of operating conditions for hydrogen polymer electrolyte fuel cells

Junxiao Wu *, Qingyun Liu, Hongbing Fang

Center for Advanced Vehicular Systems, Mississippi State University, Box 5405, Mississippi State, MS 39762-5405, USA

Received 6 May 2005; accepted 30 May 2005
Available online 25 July 2005

Abstract

A study is performed to find the optimal operating conditions of hydrogen polymer electrolyte fuel cells using an efficient optimization approach based on validated multi-resolution fuel cell simulation tool developed in house. Through the design of experiment method, a set of designed simulation runs were carried out using the fuel cell simulation tool. Based on the simulation results, an analytic metamodel was then constructed using the radial basis function approach. A feasible sequential quadratic programming scheme was then employed to optimize the metamodel to achieve the global optimal solutions. To illustrate the optimization approach, four control parameters including cell temperature, cathode stoichiometry, cathode pressure, and cathode relative humidity were considered. The optimization objective is defined as the maximization of the overall efficiency of the fuel cell system under ideal or realistic system assumptions. The study shows that different optimal solutions exist for different system assumptions, as well as different current loading levels, classified into small, medium, and large current densities. The approach adopted in this study is generic and can be readily applied to a larger number of control parameters and further to the fuel cell design optimizations.

Keywords: Optimization; Multi-resolution model; Fuel cell simulation; PEFC

1. Introduction

Numerous components and control parameters are involved for a hydrogen polymer electrolyte fuel cell (PEFC) system to operate at the optimal level. Previous studies [1,2] on the balance of plant of fuel cell systems focused on the optimization of systems consisting of fuel cell stacks, compressors, humidifiers, and cooling units. These optimization studies used phenomenon fuel cell models that were obtained through thermodynamic analysis and/or empirical data. However, due to the existence of various irreversible processes inside fuel cells and the limited availability of empirical data, the phenomenon models often yield incorrect predictions when the empirical data is not available, especially under the operating conditions with various gas humidity levels and stoichiometries. Recent experimental study [3] on hydrogen PEFCs showed that the performance of fuel cells could be greatly affected by the anode and cathode humidity levels, stoichiometries, cell temperatures, and different combinations of these conditions. Meanwhile, different fuel cell designs and materials used in the fuel cell can also have significant effects on the fuel cell performance [3]. Since phenomenon models are difficult to cover various fuel cell operating conditions and fuel cell designs, a model that captures the physics associated with each of the processes in a fuel cell has to be employed for more accurate predictions of PEFC operations.

Theoretically, the existing full three-dimensional (3D) approaches [4,5] can be employed to study the details of PEFCs, but simulations of a full size fuel cell and fuel cell stacks are prohibitive due to the unbearable computational cost. Further, for the purpose of design and operation optimization of fuel cells, the simulation turn around time has to be dramatically reduced to satisfy the industrial needs. On the other hand, some simplified models such as the

* Corresponding author. Tel.: +1 662 325 7284; fax: +1 662 325 5433.
E-mail address: jwu@cavs.msstate.edu (J. Wu).

0378-7753/$ – see front matter © 2005 Elsevier B.V. All rights reserved.
doi:10.1016/j.jpowsour.2005.05.091

Nomenclature

a	active area density ($m^2\ m^{-3}$)
A	area (m^2)
Aj_0	active catalyst area × exchange current density ($A\ m^{-3}$)
C	species mass concentration ($kmol\ m^{-3}$)
D	diffusivity ($m^2\ s^{-1}$)
E	cell potential (V)
F	Faraday constant (96,487 $C\ mol^{-1}$)
$\dot{G}$	Gibbs free energy per unit time ($J\ s^{-1}$)
g	molar Gibbs free energy ($J\ kmol^{-1}$)
h	molar water latent heat ($J\ kmol^{-1}$)
i	local current density ($A\ m^{-2}$)
I	average current density ($A\ m^{-2}$)
K	permeability of porous GDL (m^2)
L	characteristic length of the agglomerate (m)
m	molar fraction
$\tilde{m}$	gas channel mass flux rate ($kg\ m^{-2}\ s^{-1}$)
N_S	number of species
p	pressure (Pa or atm)
R	gas constant ($J\ kmol^{-1}\ K^{-1}$)
t	time (s)
T	temperature (K)
u	velocity ($m\ s^{-1}$)
V	species diffusion velocity ($m\ s^{-1}$) or cell voltage (V)
$\dot{w}$	power ($J\ s^{-1}$)
x, y, z	Cartesian coordinates (m)
Y	species mass fraction

Greek letters

α	anode transfer coefficient
β	cathodic transfer coefficient
δ	thickness of surrounding Nafion layer (m)
ε	porosity of gas diffusion layer
ϕ	membrane proton potential (V)
γ	ratio of air specific heats (1.4)
η	active overpotential (V) or efficiency
μ	viscosity ($kg\ m^{-1}\ s^{-1}$)
ρ	density ($kg\ m^{-3}$)
σ	effective ionic conductivity ($S\ m^{-1}$)
ζ	stoichiometry

Subscripts

a	anode
avg	average
c	cathode
H_2	hydrogen
hum	humidification
k	the kth species
m	membrane
O_2	oxygen
RH	relative humidity
sat	saturation
sys	system
wall	gas channel wall

empirical models [6], one-dimensional (1D) models [7,8], two-dimensional (2D) models [9–11], and quasi-3D model [12], cannot be used for systematic study of various flow and coolant channel design and optimizations due to the neglect of various channel patterns.

In this paper, the multi-resolution approach developed by Wu and Liu [13] was employed for fuel cell simulation and optimization of operating conditions for PEFCs. In the multi-resolution approach, a 3D model is employed for the membrane, in which the transport includes both convections and diffusions in all directions. The catalyst layer is modeled using a 1D + 2D model, in which at each location of the fuel cell plate, the governing equations are integrated only in the direction (1D) perpendicular to the fuel cell plate (2D). The gas diffusion layer is modeled as a 3D flow model due to the dominance of diffusion process. Modeling the flow channels presents the most challenges, because a full size, high power, single cell can have very long and complex flow channels. In the multi-resolution approach, the flow channels are represented by quasi-1D models with conservation laws satisfied at the interface between the flow channel and the gas diffusion layer.

Although the multi-resolution simulation approach reduces the simulation time to a small fraction of that of the full 3D approach, the computational time is still too high to directly combine a optimization procedure with the simulation program, because doing so would require hundreds or even thousands of sequentially performed simulations. To this end, the metamodeling approach has to be adopted to reduce the number of simulations and make optimization feasible.

In the metamodeling approach, an approximate function (metamodel) is created to replace the simulation program in optimization to obtain an output response for a given input. Since creating the metamodels only requires a limited number of predefined simulations and evaluating the metamodels is very efficient, the total cost for obtaining the optimal designs is very small. Polynomial regression has been the most common metamodeling method for years, but they are only appropriate for linear and quadratic responses. Recent studies showed that radial basis functions (RBF) were more accurate in creating models for both low- and high-order non-linear responses [14–17]. In this study, due to the high non-linearity of the fuel cell responses, the RBF models are used in our optimization of fuel cell operations.

Since this study focuses on the systematic approach to achieving the optimal operating conditions for PEFCs through multi-resolution simulation, the feasibility of the approach will be demonstrated through the optimization of

operating conditions of a single PEFC cell with control parameters including cell temperature, cathode stoichiometry, cathode gas pressure, and cathode relative humidity. The optimization with the objectives of achieving the highest fuel cell efficiencies is performed using the multi-disciplinary optimization software developed by Fang and Horstemeyer [18].

In the remaining portion of this paper, the theoretical background of the multi-resolution simulation is first given. A brief review on the RBF is then presented followed by the design optimization formulations. The simulation setup and the optimization objectives are then explained in detail. Finally, the validation of the simulation models and the analysis of the optimization are performed, followed by the conclusion.

2. Multi-resolution fuel cell simulation

In this section, the agglomerate oxygen reduction model employed for the cathode catalyst layer, the interface model for the anode catalyst layer, the porous media model for both gas diffusion layers (GDL) and the membrane layer, and the quasi-1D model for the flow channels are presented along with the related interface conditions.

2.1. Agglomerate catalyst layer model

The electrochemical reactions in the cathode catalyst layer can be symbolically expressed as

$$O_2 + 4H^+ + 4e^- \rightarrow 2H_2O. \quad (1)$$

A first order oxygen reduction mechanism is employed in association with the agglomerate model, in which the catalyst layer is treated as the collection of agglomerates consisting of carbon particle support and platinum particles surrounded by a thin layer of Nafion. In contrast to the macro-homogeneous model, which treats the catalyst layer as a homogenous phase, the agglomerate model is capable of predicting a voltage drop-off at large current densities by integrating the mass diffusion transfer resistance [13,19]. The parameters and their values used in this model are given in Table 1.

2.2. Anode catalyst layer interface model

The electrochemical reactions in the anode catalyst layer are given by

$$H_2 \rightarrow 2H^+ + 2e^-. \quad (2)$$

Hydrogen is transported to the catalyst layer through the GDL, and discharges electrons by the electrochemical reaction described in Eq. (2). The electrons move through the external circuit to provide useful current, while the protons transport through the polymer electrolyte membrane to the cathode catalyst layer and produce water by the reduction of oxygen at the cathode catalyst layer. The local current density of the anode catalyst layer i_a is modeled by the Butler–Volmer equation as [4]

$$i_a = i_{0,a}^{ref}\left(\frac{C_{H_2}}{C_{H_2}^{ref}}\right)^{\gamma_{H_2}}\left[\exp\left(\frac{\alpha_a F}{RT}\eta_a\right) - \exp\left(-\frac{\alpha_c F}{RT}\eta_a\right)\right], \quad (3)$$

where $i_{0,a}^{ref}$ is the anode reference exchange current density; $C_{H_2}^{ref}$ the anode hydrogen reference concentration; γ_{H_2} the hydrogen concentration parameter; α_a the anode anodic charge transfer coefficient; α_c is the anode cathodic charge transfer coefficient. The parameters used in Eq. (3) are listed in Table 2.

Table 1
Cathode catalyst layer parameter values

Symbol	Parameter	Values
Aj_0	Specific exchange current density ($A\,m^{-3}$)	5×10^4
β	Cathodic transfer coefficient	2
σ	Effective ionic conductivities of Nafion ($S\,m^{-1}$)	7
δ/a	Thickness of surrounding Nafion layer divided by active agglomerate area density (m^2)	6.2×10^{-12}
L	Characteristic length of the agglomerate (m)	3×10^{-6}
$D_{O_2,Nafion}^{eff} H$	Effective oxygen diffusivity in Nafion times Henry's law constant ($m^2\,s^{-1}$)	4×10^{-15}

2.3. Gas diffusion layer model

The GDL model consists of the classic Darcy's law for the velocity field and the gas phase species transport. The species transport equations are derived from those of the mass conservation laws. The governing equations of the GDL model are given as follows:

$$\varepsilon\frac{\partial \rho}{\partial t} + \nabla\cdot(\rho u) = 0, \quad (4)$$

$$u = -\varepsilon\frac{K}{\mu}(\nabla p - \rho g), \quad (5)$$

$$\varepsilon\frac{\partial \rho Y_k}{\partial t} + \nabla\cdot(\rho u Y_k) = -\nabla\cdot(\rho Y_k V_k), \quad (6)$$

Table 2
Anode catalyst layer parameter values

Symbol	Parameter	Values
$i_{0,a}^{ref}$	Anode reference exchange current density ($A\,m^{-2}$)	6×10^3
$C_{H_2}^{ref}$	Anode hydrogen reference concentration ($kmol\,m^{-3}$)	1.2
γ_{H_2}	Hydrogen concentration parameter	0.5
α_a	Anode anodic charge transfer coefficient	1
α_c	Anode cathodic charge transfer coefficient	1

where ε, ρ, u, K, μ, p, g, and Y_k are the porosity, gas phase density, super-facial velocity, permeability, effective viscosity, pressure, gravity, and the kth species mass fraction, respectively. The diffusion velocity V_k of the kth species is modeled by Fick's law as

$$Y_k V_k = -D_k^{\text{eff}} \nabla Y_k. \tag{7}$$

where D_k^{eff} is the effective kth species diffusivity and is calculated using the Bruggeman relation as

$$D_k^{\text{eff}} = \varepsilon^{1.5} D_k. \tag{8}$$

Since temperature variations in a single cell are often negligible, the isothermal condition is assumed and the energy equation is reduced to a constant temperature condition. The transport coefficients, such as the viscosity μ and the gas diffusivity D_k are computed using CHEMKIN developed at the Sandia National Laboratories [20].

2.4. Membrane model

The water transfer inside membrane is modeled to account for the convection driven by pressure gradient, electro-osmotic drag of water from the anode to the cathode, and diffusion from high to low concentration of water content. Due to the electro-neutrality assumption and the homogeneous distribution of charge sites, constant proton concentration $c^{\text{m}}_{\text{H}^+}$ in the membrane is assumed. The momentum equation takes the form of generalized Darcy relation. The potential equation is derived from Ohm's Law. The system equations for the membrane assuming isothermal condition are given as follows:

$$\frac{\partial c^{\text{m}}_{\text{H}_2\text{O}}}{\partial t} + \nabla \cdot N^{\text{m}}_{\text{H}_2\text{O}} = 0, \tag{9}$$

$$u_{\text{m}} = -\varepsilon \frac{K_{\text{m}}}{\mu_{\text{m}}} (\nabla p - \rho g), \tag{10}$$

$$\nabla \phi_{\text{m}} = -\frac{i_{\text{m}}}{\sigma_{\text{m}}} + \frac{F}{\sigma_{\text{m}}} c^{\text{m}}_{\text{H}^+} u. \tag{11}$$

Net water molar flux in the membrane is given by the Nernst–Planck equation along with the Nernst–Einstein relationship as

$$N^{\text{m}}_{\text{H}_2\text{O}} = \frac{n_{\text{d}}}{F} i_{\text{m}} - D^{\text{m}}_{\text{H}_2\text{O}} \nabla c^{\text{m}}_{\text{H}_2\text{O}} + c^{\text{m}}_{\text{H}_2\text{O}} u, \tag{12}$$

where n_{d} is the drag coefficient and $D^{\text{m}}_{\text{H}_2\text{O}}$ is the water self-diffusion coefficient.

2.5. Quasi-1D channel model

The gas channel model is developed from the mass and momentum conservation laws with variables changing only in the flow direction. The governing equations for the multi-component, non-reactive gas mixture can be written as

$$\frac{\text{d}}{\text{d}t} \int_{\text{d}v} \boldsymbol{Q} \, \text{d}v + \boldsymbol{F}_2 A_2 - \boldsymbol{F}_1 A_1 = \boldsymbol{S}, \tag{13}$$

where A_1 and A_2 are inlet and outlet areas and $\boldsymbol{F}_1$ and $\boldsymbol{F}_2$ are fluxes through the flow areas. The vectors $\boldsymbol{Q}$, $\boldsymbol{F}$, and $\boldsymbol{S}$ are given by

$$\boldsymbol{Q} = \begin{bmatrix} \rho Y_k \\ \rho \\ \rho u \end{bmatrix}, \qquad \boldsymbol{F} = \begin{bmatrix} \rho Y_k u - \rho D_k \nabla Y_k \\ \rho u \\ \rho u^2 + p - \mu \nabla u \end{bmatrix},$$

$$\boldsymbol{S} = \begin{bmatrix} \displaystyle\int_{A_{\text{wall}}} \tilde{m}_k \, \text{d}A \quad (k = 1, N_{\text{S}} - 1) \\ \displaystyle\sum_{k=1}^{N_{\text{S}}} \int_{A_{\text{wall}}} \tilde{m}_k \, \text{d}A \\ f_{\text{wall}} \end{bmatrix}, \tag{14}$$

where A_{wall} is the wall area. Eq. (14) takes into account the effects of the species mass transport and the channel viscous friction.

2.6. Boundary and interface conditions

The inlet velocities, temperatures, and species mass fractions of the anode and cathode need to be specified. At the outlets of the gas channel, only the backpressure is specified with an extrapolated boundary condition employed for other variables. Non-slip boundary condition is specified at all external surfaces.

For the bipolar solid wall, a non-slip boundary condition is employed, and no species mass transport is allowed. The detailed formulation of the quasi-1D boundary conditions can be found in Ref. [13].

At the interface between the GDL and the gas channel, the GDL provides the mass flux including both mass convection and diffusion, and the gas channel provides the GDL with the values of dependent variables including the pressure and species concentrations. The viscous friction is calculated the same way as the solid wall, because the velocity at the interface is almost zero and much smaller than the mean channel velocity.

The interface conditions between the GDL and the catalyst layer are implemented as the following. For the GDL, the kth species mass flux f_k including both the mass convection and diffusion through the interface is given as

$$(\rho u Y_k - D_k^{\text{eff}} \nabla Y_k)|_{\text{GDL}} = f_k. \tag{15}$$

At the anode side, the hydrogen consumption flux based on the local current density is given as

$$f_{\text{H}_2} = -\frac{M_{\text{H}_2}}{2F} i_{\text{a}}, \tag{16}$$

where i_{a} is the anode catalyst local current density. Water flux at the interface is given as Eq. (12). At the cathode, oxygen

flux due to reaction is given as

$$f_{O_2} = -\frac{M_{O_2}}{4F} i_c, \tag{17}$$

where the local current density i_c is calculated through the cathode agglomerate model. Besides the water transfer due to electro-osmotic drag, water created due to electrochemical reaction at the catalyst layer is given as

$$S_{H_2O} = \frac{M_{H_2O}}{2F} i_c. \tag{18}$$

The total water flux at cathode catalyst layer interface is then given as

$$f_{H_2O} = S_{H_2O} + N^{m}_{H_2O}. \tag{19}$$

It is assumed that the water in the GDL is in equilibrium with that in the membrane layer at the interface, which implies that the water activity is same for both membrane and GDL at the interface.

The membrane potential equation is solved by obtaining the local current density at the cathode side together with the potential value at the anode side. The cathode current density is calculated through the cathode agglomerate model, while the potential at the anode side is set as the anode activation overpotential. In many previous studies, the activation overpotentials of anode and cathode are specified as constants. But in this paper, they are computed and updated iteratively, which results in more accurate prediction of the local current density.

The fuel cell reversible open circuit voltage is calculated as [21]

$$E_{rev} = 1.23 - 0.9 \times 10^{-3}(T - 298.15) + \frac{RT}{2F}(\ln P_{H_2} + \frac{1}{2} \ln P_{O_2}) \tag{20}$$

where P_{H_2} and P_{O_2} are the partial pressure of hydrogen at the anode inlet and the partial pressure of oxygen at the cathode inlet, respectively. After the initialization of the cathode activation overpotential, an initial cathode current density is obtained. Further, the anode activation overpotential is updated according to Eq. (3). The membrane potential equation is solved to obtain the membrane ohmic overpotential η_{ohm} and finally the cathode overpotential is updated as

$$\eta_c = E_{cell} - E_{rev} - \eta_a - \eta_{ohm}, \tag{21}$$

where E_{cell} is the specified cell potential.

This algorithm is capable of predicting the average cell current density based on the specified cell potential or cell potential based on the specified average cell current density. Either the flow rates or the stoichiometry can be specified for the simulation. The data flowchart among the related modules for predicting the average cell current density based on specified cell potential and stoichiometry is shown in Fig. 1.

3. Metamodeling and optimization

Optimization is a reverse engineering process to find the input parameters corresponding to the optimal output responses. This process is iterative and typically involves a large number of calculations to obtain output responses based on given inputs. For fuel cell applications, the input–output relationships are not available in explicit form and must be obtained through simulations that are computationally expensive. To make optimization feasible and efficient, the metamodeling approach has to be adopted to represent the input–output relationships with approximation functions (metamodels) that are in explicit form and less expensive to evaluate. Optimization is then performed on metamodels to find the optimal solutions. Since creating metamodels only requires a limited number of predefined simulations (sampling points), the total computational cost is very small.

3.1. Metamodeling with radial basis functions

The RBF was originally developed by Hardy [22] to fit large and non-linear data sets and was shown to produce good approximations. However, recent studies showed that the RBF was also appropriate for both low- and high-order non-linear responses with limited samplings [14–17].

An augmented RBF model has the form of

$$f'(\boldsymbol{x}) = \sum_{i=1}^{n} \lambda_i \phi(\|\boldsymbol{x} - \boldsymbol{x}_i\|) + \sum_{j=1}^{p} c_j g_j(\boldsymbol{x}), \tag{22}$$

where n is the number of sampling points, $\boldsymbol{x}$ a vector of design variables (input parameters), $\boldsymbol{x}_i$ a vector of design variables at the ith sampling point, $||\boldsymbol{x} - \boldsymbol{x}_i||$ the Euclidean norm, ϕ a basis function, λ_i the coefficient to be determined for the ith basis function, $g(\boldsymbol{x})$ a linear polynomial function, p the total number of terms in the polynomial, and c_j is the coefficient to be determined. In this study, the Wu's compactly supported function $\phi_{3,0}$ [23] is used in creating all the response functions and is given by

$$\phi_{3,0}(t) = (1-t)^7(5 + 35t + 101t^2 + 147t^3 + 101t^4 + 35t^5 + 5t^6) \tag{23}$$

where t is the normalized Euclidean norm ($t = ||\boldsymbol{x} - \boldsymbol{x}_i||/\max(||\boldsymbol{x}_k - \boldsymbol{x}_i||)$, $k = 1, 2, \ldots, n$). Eq. (22) is underdetermined, because there are more parameters to be solved than the number of equations created with available data points. Therefore, the orthogonality condition is further imposed on coefficients $\boldsymbol{\lambda}$ so that

$$\sum_{i=1}^{n} \boldsymbol{\lambda}_i g_j(\boldsymbol{x}_i) = 0, \quad \text{for } j = 1, 2, \ldots, p. \tag{24}$$

By replacing $\boldsymbol{x}$ and $f'(\boldsymbol{x})$ in Eq. (22) with the n vectors of design variables and corresponding function values and combining with Eq. (24), we obtain $(n+p)$ equations in the matrix format

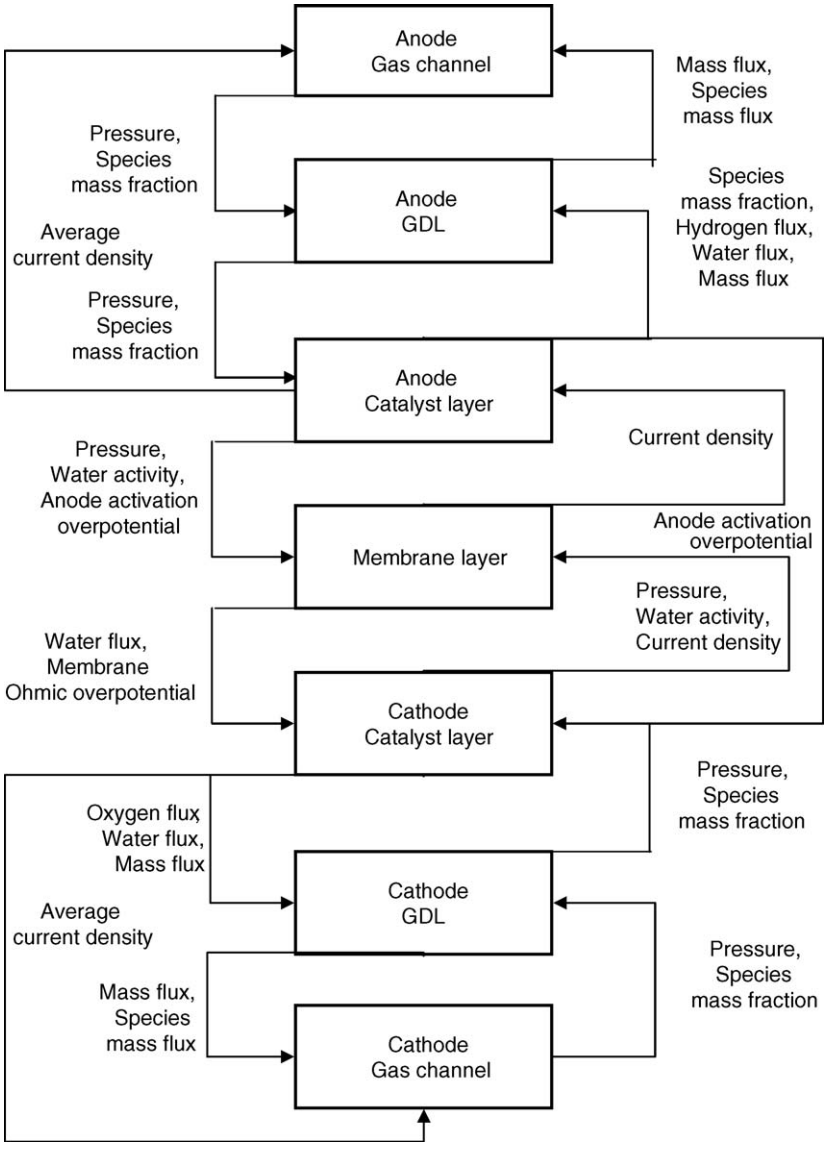

Fig. 1. Data flowchart among related modules for the multi-resolution simulation.

as

$$\begin{pmatrix} \boldsymbol{A} & \boldsymbol{G} \\ \boldsymbol{G}^{\mathrm{T}} & 0 \end{pmatrix} \begin{pmatrix} \boldsymbol{\lambda} \\ \boldsymbol{c} \end{pmatrix} = \begin{pmatrix} \boldsymbol{f} \\ 0 \end{pmatrix}, \tag{25}$$

where $\boldsymbol{A}_{i,j} = \phi(||\boldsymbol{x}_i - \boldsymbol{x}_j||)$ $(i = 1, 2, \ldots, n, j = 1, 2, \ldots, n)$, $\boldsymbol{G}_{i,j} = g_j(\boldsymbol{x}_i)$ $(i = 1, 2, \ldots, n, j = 1, 2, \ldots, p)$, $\boldsymbol{\lambda} = [\lambda_1, \lambda_2, \ldots, \lambda_n]^{\mathrm{T}}$, $\boldsymbol{c} = [c_1, c_2, \ldots, c_p]^{\mathrm{T}}$, and $\boldsymbol{f} = [f'(\boldsymbol{x}_1), f'(\boldsymbol{x}_2), \ldots, f'(\boldsymbol{x}_n)]^{\mathrm{T}}$. Solving Eq. (25) gives the coefficients $\boldsymbol{\lambda}$ and $\boldsymbol{c}$ for the RBF function in Eq. (22).

3.2. Optimization formulation and solution

The optimization problem of this study is to achieve optimal operating conditions in terms of PEFC efficiencies under small, medium, and large electrical currents, respectively. Four control parameters (design variables) are selected in this study; they are the cell temperature, cathode stoichiometry, cathode gas pressure, and cathode relative humidity. The optimization problem consists of three tasks each of which can be formulated as

Find $\boldsymbol{x}$ which maximizes $f(\boldsymbol{x})$ subject to the constraints

$$x_i^{\mathrm{L}} \le x_i \le x_i^{\mathrm{U}}, \quad i = 1, 4 \tag{26}$$

where $f(\boldsymbol{x})$ is the efficiency function obtained through meta-modeling, and x_i^{L} and x_i^{U} are the lower and upper bounds of the ith design variable, respectively.

The gradient-based feasible sequential quadratic programming (FSQP) method [24] is used for this optimization problem. Since the RBF models for the objectives are typically highly non-linear functions, the FSQP method can easily be trapped into local optima with a single starting point. To avoid this problem, a number of random starting points are used in solving each of the optimiza-

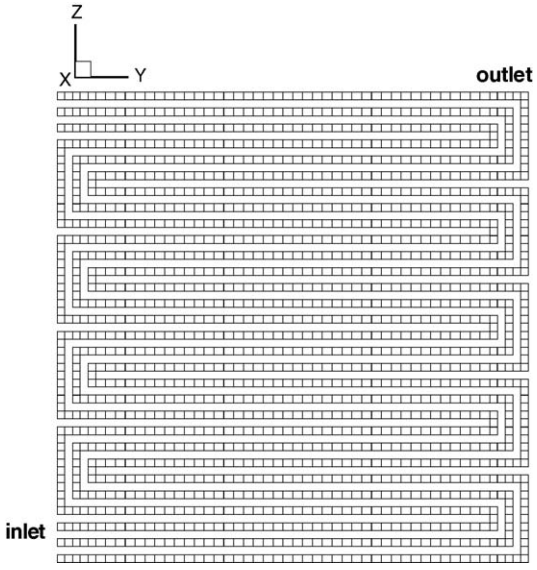

Fig. 2. The grid of the three-channel serpentine gas flow channel employed for both the anode and cathode sides.

tion tasks, and the best solution is chosen as the final optimum.

4. Simulation setup

The simulations were carried out for a typical 25 cm^2 PEFC with three channel serpentine flow patterns for both the cathode and anode sides with co-flow arrangement. Fig. 2 shows the gas channel grid, generated using the parametric grid generation code developed in house. The channel height, width, rib width, and number of inlet and channel turns are used as parameters for the specific grid generations. The channel height, width, and rib width are set as 1, 1, and 1.2 mm, respectively. The grid size for the cathode GDL, the membrane layer and the anode GDL are all $10 \times 51 \times 51$. The overall active area of the fuel cell is 50 mm × 50 mm. The physical parameters of GDL and membrane layer (Nafion 115) used in this simulation are listed in Table 3.

To ease the analysis, four parameters, including the cathode pressure, relative humidity, stoichiometry, and the cell temperature, were chosen to adjust the fuel cell operations, while the anode pressure, relative humidity and stoichiometry were fixed at 1.0 atm, 100% and 1.5, respectively. The ranges of each parameter shown in Table 4 were selected based on the previous experience of fuel cell operations. Using the advanced design of experiment method, instead of thousands of simulation runs, only 75 simulation runs were conducted in parallel for the optimization of operating conditions.

Table 3
Physical parameters of GDL and membrane layer

Symbol	Parameter	Values
ε	GDL porosity	0.5
K	GDL permeability (m^2)	1.0×10^{-12}
δ	GDL thickness (mm)	0.3302
ε_m	Membrane porosity	0.5
K_m	Membrane permeability (m^2)	1.8×10^{-18}
μ_m	Membrane effective viscosity ($kg\,m^{-1}\,s^{-1}$)	8.91
ρ^m_{dry}	Dry membrane density ($kg\,m^{-3}$)	2000
M^m	Membrane molecular mass ($kg\,kmol^{-1}$)	1100
$c^m_{H^+}$	Proton concentration ($kmol\,m^{-3}$)	1.2
δ_m	Membrane thickness (mm)	0.1778

Table 4
Operating parameter ranges and values

Symbol	Parameter	Range or value
T	Cell temperature (°C)	50–90
ζ_c	Cathode stoichiometry	1.1–5
ζ_a	Anode stoichiometry (fixed)	1.5
p_c	Cathode pressure (atm)	1–5
p_a	Anode pressure (atm) (fixed)	1
RH_c	Cathode relative humidity (%)	10–100
RH_a	Anode relative humidity (%) (fixed)	100

Many possible optimization objectives exist for different applications. Though the current approach is generic with various objectives, for the purpose of simplifying the analysis and discussion, the optimization objective of this study is chosen as the maximization of the fuel cell efficiencies under the average current density loadings of 0.15, 0.45, and 0.75 $A\,cm^{-2}$ to represent small, medium, and large current density loadings, respectively.

The efficiency η_{sys} of the system, consisting of a single cell, humidifier, and air compressor, is defined as

$$\eta_{sys} = \frac{A I_{avg} V_{cell}}{\dot{G} + \dot{w}_{hum} + \dot{w}_{compressor}}, \tag{27}$$

where A, I_{avg}, and V_{cell} are the fuel cell active area, average current density and cell voltage, respectively. The maximum work done per unit time through consumption of equal amount of hydrogen under reversible conditions is the Gibbs free energy per unit time $\dot{G}$ expressed as:

$$\dot{G} = \frac{A I_{avg} g_{H_2}}{2F[\zeta_a + (\zeta_a - 1)\eta_R]} \tag{28}$$

where g_{H_2}, ζ_a, and η_R are the hydrogen molar Gibbs free energy, anode stoichiometry and hydrogen recycle efficiency. $\dot{w}_{hum}$ and $\dot{w}_{compressor}$ are the power done to humidify the anode and cathode inlet streams, and to compress the air from ambient pressure to cathode inlet pressure [25], respectively:

$$\dot{w}_{hum} = \frac{A I_{avg} h_L}{\eta_{hum} F} \times \left[\frac{\zeta_c p_{sat} RH_c}{4(p_c - p_{sat} RH_c) x^{O_2}_{air}} + \frac{\zeta_a p_{sat} RH_a}{2(p_a - p_{sat} RH_a)} \right] \tag{29}$$

$$\dot{w}_{compressor} = \frac{A I_{avg} c_p T_{ambient}}{4F \eta_{compressor} x^{O_2}_{air}} \left[\left(\frac{p_c}{p_{ambient}} \right)^{\gamma/\gamma - 1} - 1 \right] \tag{30}$$

where ζ_c, h_L, p_{sat}, $x_{air}^{O_2}$, η_{hum}, and $\eta_{compressor}$ are the cathode stoichiometry, molar latent heat of water, water saturation pressure at the cell temperature, molar fraction of oxygen in dry air, humidifier, and isentropic compressor efficiency, respectively. In addition, RH_c and RH_a are the cathode and anode relative humidity, respectively. Here, $\dot{w}_{compressor}$ is computed assuming the mechanical efficiency of the compressor to be unit according to Larminie and Dicks [25]. Since the anode side conditions are fixed in current study, the hydrogen compression work required is not considered and also hydrogen is assumed to be fully recycled. In addition, it is assumed that the only useful work done by the fuel cell is electric power and no heat co-generation is considered for the low temperature operation of fuel cells.

5. Results and discussion

The single phase multi-resolution fuel cell simulation framework developed in house has been validated against the experimental data under different operating conditions when flooding is not a serious factor. Similar to the approach used by Springer et al. [7], the liquid water is treated as super gas. As shown in Fig. 3, the numerical predictions and the experimental measurements for different cathode relative humidities are in good agreement. The details of the validation and accuracy analysis of the simulations can be found in Ref. [26].

5.1. Fuel cell performance under different operating conditions

The fuel cell might be operated at different range of average current densities for different applications. For example, if the fuel cell efficiency and the stable performance of fuel cells are required, fuel cells might be loaded at lower current density range. If the high power output is required, fuel cells might be operated under medium-range current density loading. However, if high current output is required, fuel cells will tend to be operated close to the limiting current, constrained of course by the stability of the system.

Under different current loadings, the effects of each operating parameter on the fuel cell performance are different. For example, from Fig. 4, showing the effect of the cathode

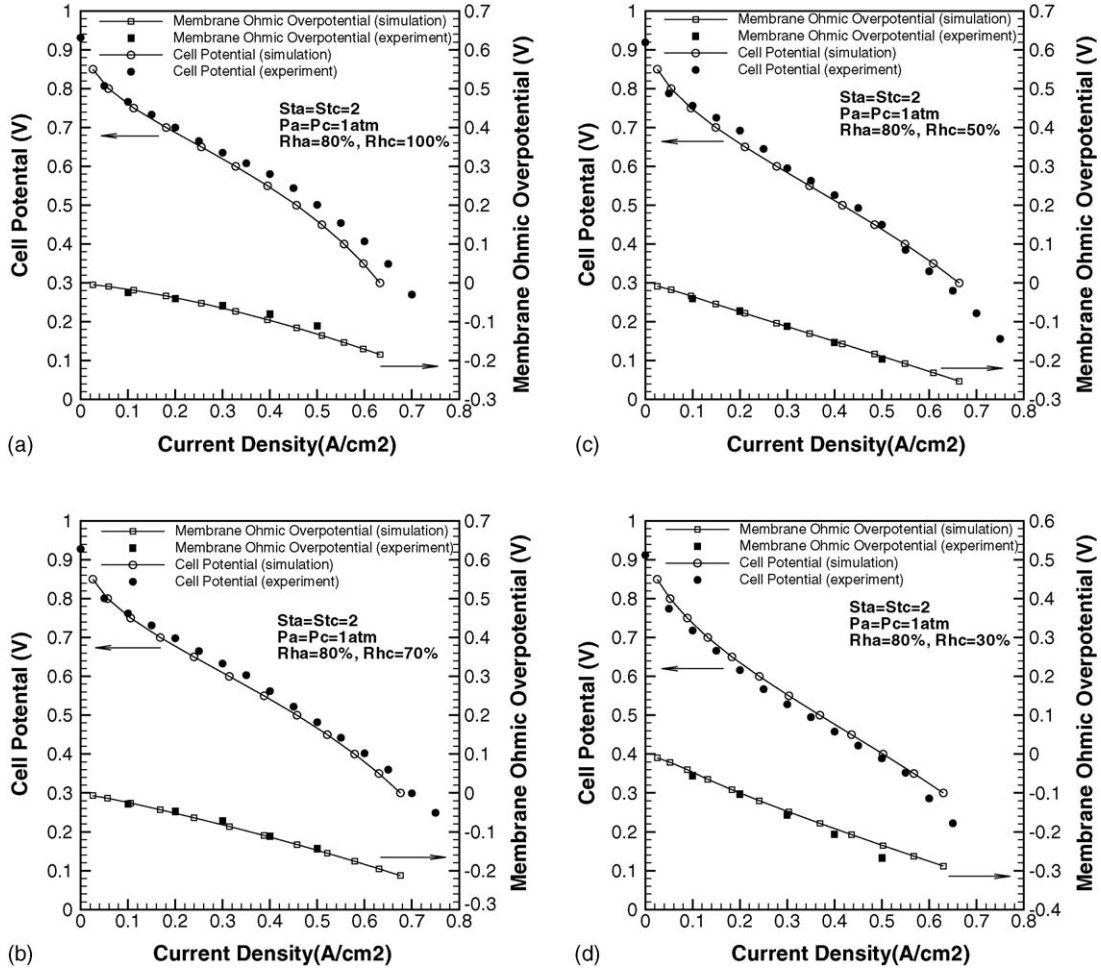

Fig. 3. Comparison of polarization curves and membrane ohmic overpotential for different cathode inlet air RH, while maintaining anode at 80% relative humidity. Cathode inlet air RH (a) 100%; (b) 70%; (c) 50%; (d) 30%.

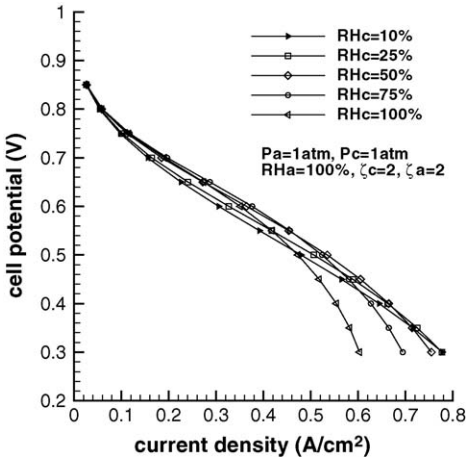

Fig. 4. Comparison of polarization curves for different cathode inlet air RH, while maintaining a fully humidified anode inlet condition.

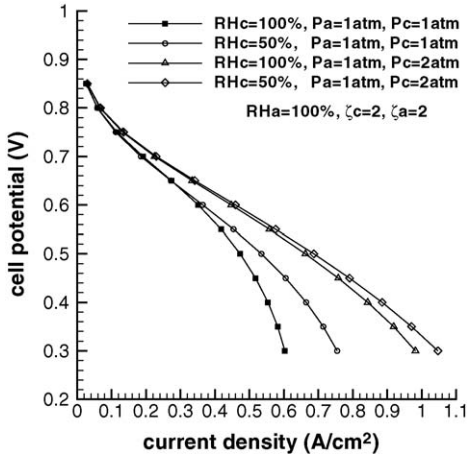

Fig. 6. Comparison of polarization curves for different operating pressures and cathode inlet air relative humidity.

relative humidity on fuel cell performance, high cathode relative humidity tends to reduce the fuel cell performance at large current density when excessive water is generated and cannot be removed quickly. On the other hand, at medium current density, when the sufficiency of the oxygen and the membrane hydration status generally determine the fuel cell performance, the high relative humidity can either adversely affect the fuel cell performance due to the decrease in oxygen supply or favorably due to the increase in membrane conductivity. At low current density, when ohmic potential is negligible, the high relative humidity often tends to adversely affect the fuel cell performance due to low oxygen partial pressure, though at very small magnitude. In addition, different combinations of the operating conditions also play an important role in the fuel cell performance. If the cathode oxygen stoichiometry is increased from 2 to 10, the effect of cathode relative humidity on cell performance changes as shown in Fig. 5, since the sufficiency of oxygen is not a factor under high stoichiometry and only the membrane hydration status determines the fuel cell performance.

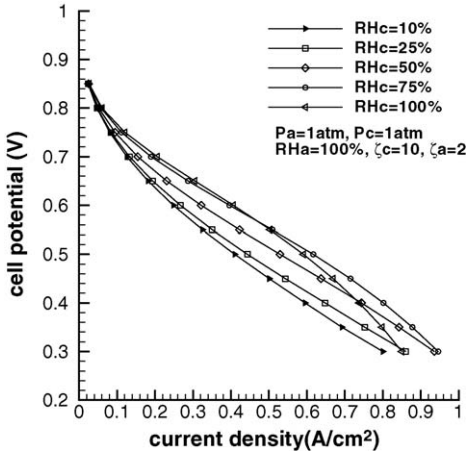

Fig. 5. Comparison of polarization curves for different cathode inlet air RH, increasing the cathode stoichiometry to 10, while maintaining a fully humidified anode inlet condition.

Though parameters such as the relative humidity may have different effects on fuel cell performance under different conditions, the increase of cathode pressure increases the fuel cell performance in general as shown in Fig. 6. However, the increase of cathode pressure comes at the cost of work done by the compressor. In reality, the favorable effect of high cathode pressure can also be compromised by the compressor noise level and gas sealing requirements, which are not considered in the current study for ease of analysis, though.

5.2. Optimization of fuel cell operating conditions

Since detailed simulations of auxiliary components such as humidifier and air compressor are not considered, as they are not the focus of the current study, their efficiencies are assumed. To evaluate the effects of auxiliary component efficiency on the overall system efficiency, an ideal system, in which the work done by all the auxiliary components are neglected, is first assumed. Then, to simplify the analysis but without losing generality, the humidifier and air compressor efficiencies are assumed both at 50%. Table 5 shows the optimization results of the ideal case. As expected, the

Table 5
Optimization results under ideal condition

Parameter	Current density		
	0.15 A cm^{-2}	0.45 A cm^{-2}	0.75 A cm^{-2}
Cell temperature (°C)	51.1	61.8	90
Cathode stoichiometry	3.88	5	5
Cathode pressure (atm)	3.28	5	5
Cathode relative humidity (%)	10.6	10	75.2
Efficiency (true value)	0.618	0.492	0.393
Efficiency (prediction)	0.619	0.495	0.412
Error (%)	0.31	0.67	4.68

optimal efficiency drops as the current loading increases due to the increase in total overpotential that consists of activation, ohmic, and concentration contributions. In general, the activation overpotential only increases slightly with the change of current density while the ohmic overpotential increases linearly when the membrane hydration status does not vary much, and the concentration overpotential will increase dramatically near and at the limiting current density. Since no compressor cost is involved, the fuel cell operation optimization is achieved near or at the higher bound of the specification ranges of the cathode pressure and stoichiometry for all three levels of current density loadings.

The optimal cell temperature lies in the lower bound of the specification range for small and medium current density loadings due to the fact that fuel cell open circuit voltage and thus the cell voltage increase as the cell temperature decreases from Eq. (20). However, at large current densities, the fuel cell voltage is more influenced by the transport properties inside the fuel cells and as a result, the optimal cell temperature for the large current density loading is at the higher bound of the specification range, in which the flooding effect is more likely to be reduced due to high water saturation pressure at high temperature. In addition, low cathode relative humidity optimizes the fuel cell efficiency at small and medium current densities while relative high relative humidity optimizes the fuel cell efficiency at large current density shown also in Table 5. The result is actually the complex interplay of all the control parameters. At small and medium current density, the increase in partial pressure of oxygen greatly increases the fuel cell performance through reducing the activation overpotential; however, at large current density, since the optimal cell temperature is shown to be at the high end of the specification rage, the membrane hydration status and thus the proton conductivity plays a more important role: the increase in relative humidity tend to hydrate the membrane and thus reduce the ohmic overpotential.

To validate the optimization results, the simulations with the predicted optimal parameter values were carried out and the true system efficiencies were then obtained for the three different current loadings, respectively. The comparison between the true efficiency and predicted optimal efficiency is also shown in Table 5 for the ideal case. As we can see that the maximum prediction error is only 4.68% for the large current loading case. Generally speaking, the prediction error depends on the non-linearity of the response functions and can be improved by increasing the number of sampling points.

Table 6 shows the optimization result of the case in which the air compressor and humidifier efficiencies are both set at 50%. Understandably, the system efficiencies for all the loadings have dropped compared to the ideal case, and especially for the large loading case, of which the system efficiency has dropped around 35%. It can also be seen that the optimal values for the four control parameters have changed greatly. Due to the consideration of the work done by the air compressor and humidifier, the optimal values for the cathode stoichiometry, cathode pressure, and cathode relative humidity tend to be at the lower bound of the specification ranges. The variation of optimal values for the cell tem-

Table 6
Optimization results under realistic condition

Parameter	Current density		
	0.15 A cm^{-2}	0.45 A cm^{-2}	0.75 A cm^{-2}
Cell temperature (°C)	50.2	55.5	70.4
Cathode stoichiometry	1.34	1.53	1.85
Cathode pressure (atm)	1.69	2.46	2.94
Cathode relative humidity (%)	15.9	10.4	12.6
Efficiency (true value)	0.523	0.374	0.258
Efficiency (prediction)	0.522	0.374	0.265
Error (%)	−0.15	0.09	2.67

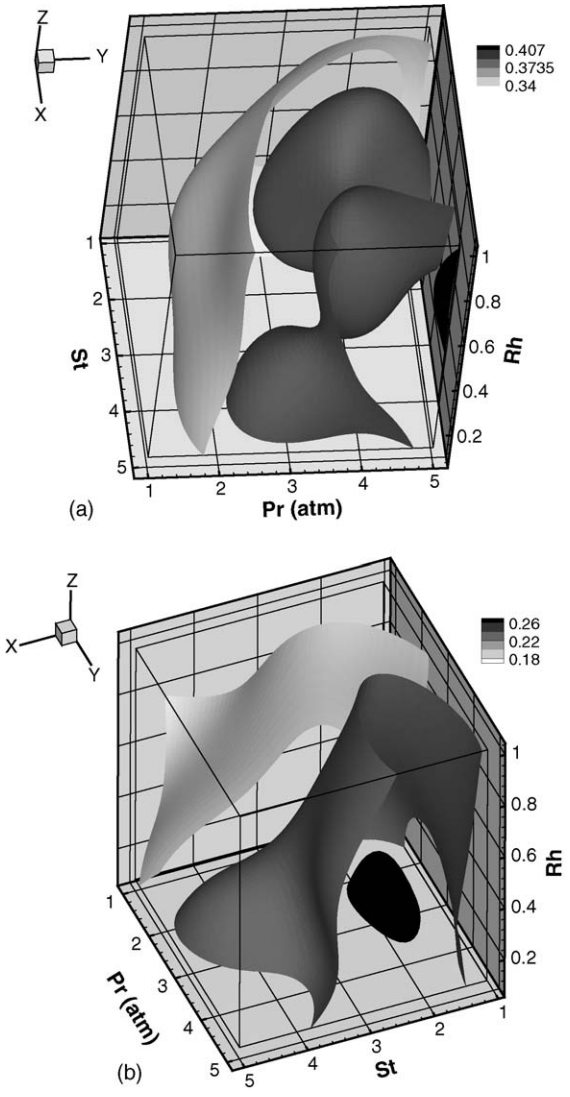

Fig. 7. System efficiency iso-surface plots under large current density loading with the cell temperature fixed at the predicted optimal values for the ideal and realistic system cases, respectively. (a) Ideal systems and (b) realistic systems.

perature with the current loading levels still maintains the same trend as the ideal case though the optimal cell temperature value at large current density loading drops from the higher bound to the middle of the specification range. Similar to the ideal case, the comparison between the true value and the prediction of the system efficiency shows that the optimization result is accurate with maximum error at only 2.67% and the number of simulation runs should be sufficient.

For the purpose of illustrating the difference between the ideal and realistic response functions, Fig. 7 shows the three level iso-surfaces of the ideal and realistic response functions under large current loading with the cell temperature fixed at the predicted optimal values, respectively. Essentially, the iso-surface plots, with x-, y-, z-axis being the cathode stoichiometry, cathode pressure, and relative humidity, respectively, exhibit the path toward the optimal solutions for each case. It can also be seen that the objective function (system efficiency) for the ideal case under large current density loading is much more irregular than the corresponding realistic case, which also explains the larger prediction error for the ideal case.

6. Conclusion

An efficient and systematic approach to achieving the optimal operating conditions for PEFCs has been developed. The validated multi-resolution fuel cell simulation tool developed in house has been utilized to carry out a specified number of simulations designed by using the design of experiment method. Due to the high irregularity of the model describing the overall fuel cell system efficiency as a function of the four control parameters including cell temperature, cathode stoichiometry, cathode pressure, and relative humidity, the radial basis function approach for constructing the approximation function or metamodel is employed instead of the polynomial regression approach that is only suitable for regular models. In order to achieve the global optimization, the feasible sequential quadratic programming method is modified by starting from a set of randomly picked initial points. The overall system efficiency defined under either ideal or realistic system conditions is used as the objective function. Three typical levels of current loadings 0.15, 0.45, and 0.75 A cm^{-2} are considered to represent small, medium and large current loadings.

The fact that the predicted optimization results are in good agreement with the true values demonstrates the accuracy and validity of the approach. Different optimal solutions exist for different system assumptions as well as different current loadings. Under the ideal system assumptions in which the work done by the auxiliary components are neglected, the highest efficiencies under different current loadings tend to be achieved near or at the higher bound of the specification ranges of the cathode stoichiometry and pressure. However, under the realistic conditions in which the work done by the humidifier and the air compressor is considered, the optimal choice for the four control parameters to achieve the highest system efficiency changes and the maximum system efficiency also drops.

The approach developed herein is neither restricted to only four control parameters nor to the fuel cell operation optimizations. The approach will be readily applied to the fuel cell design optimizations in the future. When the number of control parameter increases, especially for the design optimization applications, the design of experiment approach can ensure that the number of simulation runs needed to stay within reach. However, an approximate estimation of required number of simulation runs as a function of number of control parameters is needed to achieve certain accuracy level.

Acknowledgement

The authors acknowledge the support of the Center for the Advanced Vehicular Systems (CAVS), Mississippi State University.

References

[1] J. Godat, F. Marechal, J. Power Sources 118 (2003) 411–423.
[2] C.N. Maxoulis, D.N. Tsinoglou, G.C. Kotsakis, Energy Convers. Manage. 45 (2004) 559–573.
[3] M.V. Williams, H.R. Kunz, J.M. Fenton, J. Power Sources 135 (2004) 122–134.
[4] S. Um, C.-Y. Wang, K.S. Chen, J. Electrochem. Soc. 147 (2000) 4485–4493.
[5] S. Um, C.-Y. Wang, J. Power Sources 125 (2004) 40–51.
[6] R.F. Mann, J.C. Amphlett, M.A. Hooper, H.M. Jensen, B.A. Peppley, P.R. Roberge, J. Power Sources 86 (2000) 173–180.
[7] T.E. Springer, T.A. Zawodzinski, S. Gottesfeld, J. Electrochem. Soc. 138 (1991) 2334–2342.
[8] D.M. Bernardi, M.W. Verbrugge, AIChE J. 37 (1991) 1151–1163.
[9] T.F. Fuller, J. Newman, J. Electrochem. Soc. 140 (1993) 1218–1225.
[10] T.V. Nguyen, R.E. White, J. Electrochem. Soc. 140 (1993) 2178–2186.
[11] J.S. Yi, T.V. Nguyen, J. Electrochem. Soc. 145 (1998) 1149–1159.
[12] A.A. Kulikovsky, Numer. Meth. Program. 3 (2002) 150–160.
[13] J. Wu, Q. Liu, J. Fuel Cell Sci. Technol. 2 (2005) 20–28.
[14] H. Fang, M.F. Horstemeyer, Eng. Optimization, in press.
[15] H. Fang, M. Rais-Rohani, Z. Liu, M.F. Horstemeyer, Comput. Struct., in press.
[16] R. Jin, W. Chen, T.W. Simpson, Struct. Multidisciplinary Optimization 23 (2001) 1–13.
[17] T. Krishnamurthy, The 44th AIAA/ASME/ASCE/AHS/ASC Structures, Structural Dynamics, and Materials Conference, Paper No. AIAA-2003-1748 Norfolk, VA, 2003.
[18] H. Fang, M.F. Horstemeyer, Proceedings of the 10th AIAA/ISSMO Multidisciplinary Analysis and Optimization Conference, Paper No. AIAA-2004-4499 Albany, NY, 2004.
[19] K. Broka, P. Ekdunge, J. Appl. Electrochem. 27 (1997) 281–289.
[20] R.J. Kee, F.M. Rupley, J.A. Miller, SAND 89-8009B, Sandia National Laboratories, 1989.
[21] C.-Y. Wang, Chem. Rev. 104 (2004) 4727–4766.

[22] R.L. Hardy, J. Geophys. 76 (1971) 1905–1915.
[23] Z. Wu, Adv. Comput. Math. 4 (1995) 283–292.
[24] C.T. Lawrence, J.L. Zhou, A.L. Tits, User's guide for CFSQP, Ver2.5, Electrical Engineering Department and Institute for Systems Research, University of Maryland, College Park, MD, 1997.
[25] J. Larminie, A. Dicks, Fuel Cell Systems Explained, first ed., John Wiley & Sons Inc., New York, 2000, p. 235.
[26] Q. Liu, Q. Yan, J. Wu, Proceedings of the 3rd International Conference on Fuel Cell Science, Engineering and Technology, FUELCELL2005-74088 Ypsilanti, MI, 2005.